ZINC DIPHOSPHATE $Zn_2P_2O_7$ GLASS: ELABORATION, CHARACTERIZATION, AND DFT STUDY

Abdelahad El Addali[1], Abdellah El Boukili[1], Lahcen Boudad[2], M'hamed Taibi[1]

[1]*Mohammed V University in Rabat, Centre Sciences des Matériaux*
Laboratoire de Physico-Chimie des Matériaux Inorganiques et Organiques (LPCMIO)
Ecole Normale Supérieure Rabat BP : 8007. (U.M.5) Morocco, hioaddali@gmail.com (A.A.),
abdellahelboukili@gmail.com (A.B.), taibiens@yahoo.fr (T.M).
[2]*Engineering Laboratory of Organometallic, Molecular Materials, and Environment*
Faculty of Sciences, University Sidi Mohamed Ben Abdellah
Fez 30000, Morocco, lahcen.boudad@um5s.net.ma (L.B)

Received 14 January 2025
Accepted 12 April 2025 *DOI: 10.59957/jctm.v61.i3.2026.10*

ABSTRACT

Zinc diphosphate glass $Zn_2P_2O_7$ has been synthesized using the conventional melt quenching process and investigated through various techniques. These analyses include X-ray diffraction (XRD), differential scanning calorimetry (DSC), Fourier-transform infrared spectroscopy (FT-IR), and Raman spectroscopy. Besides confirming the glassy nature of this material, the different phosphate groups within the glass structure have been identified and their vibration frequencies have been assigned. The study aims to propose three distinct short-range structural models for the $Zn_2P_2O_7$ glass compound: ^{IV}Zn, ^{V}Zn, and ^{VI}Zn. These buildings underwent optimization and a detailed theoretical analysis using the Density Functional Theory (DFT) method. By examining the global reactivity indices of these clusters, we were able to identify the most stable structural configuration for this compound. The results of the investigation confirm a strong agreement between the experimental observations and theoretical predictions, enhancing our understanding of the material's structure.

Keywords: DSC, DFT, diphosphate glass, FT-IR, Raman spectroscopy, global reactivity indices, XRD.

INTRODUCTION

Zinc diphosphate glasses are materials of substantial technological relevance, widely studied for their diverse applications. This includes their use in dental implants [1 - 6], bone fracture fixation [7, 8], and drug delivery devices [9, 10]. Notably, these glasses demonstrate a notable capacity for housing proton carriers at mid-range temperatures, positioning them as a promising candidate for use as a solid electrolyte in fuel cells [11,12]. Furthermore, the diphosphate glasses exhibit potential as a host material for controlled-release fertilizers [13 - 16].

The connections between oxygen atoms and cations mainly exhibit ionic characteristics, pointing towards the formation of a chelate-type complex between cations and phosphate tetrahedra [17]. The vitreous network can also contain intermediate oxides, such as ZnO, whose formative nature enables the cross-linking of the network through predominantly covalent bonds with phosphate groups. The zinc phosphate system is particularly interesting due to its ease of glass formation, allowing for the incorporation of ZnO contents that exceed the compositional limit of pyrophosphate. The structure of zinc diphosphate glass is formed by phosphate tetrahedra (PO_4), which are isolated or linked to other phosphate tetrahedra. The structure of this glass network is effectively described using the notation Q_i, where Q represents the phosphate tetrahedron, and i represents the number of neighbouring P tetrahedra connected by a common oxygen bridge [18, 19].

To improve the physical attributes and chemical resilience of diphosphate glasses, recent studies have focused on incorporating different heavy metal oxides into the P_2O_5 glass matrix [20 - 23]. The integration of zinc oxide (ZnO) into P_2O_5 glass specifically results in

the disruption of some P-O-P bonds within the glass structure, leading to an increase in non-bridging oxygen (NBO) atoms. However, several studies have shown that the introduction of zinc oxides into diphosphate glasses allows the substitution of P-O-P bonds with P-O-Zn ones, which exhibit more chemical durability [24].

In this research, which combines both experimental and theoretical approaches, we investigated into the structural characteristics of $Zn_2P_2O_7$. Our study involved experimental techniques and theoretical modelling using Density Functional Theory (DFT). We confirmed the glass-like nature of our sample using X-ray diffraction (XRD) and Differential Scanning Calorimetry (DSC). The structural details were further examined through Fourier-transform infrared (FT-IR) and Raman spectroscopy. Through a detailed examination of FT-IR and Raman spectra, we have established a clear link between zinc and the Q_1 unit. This key discovery led us to use Density Functional Theory (DFT) for analysing the short-range structure of $Zn_2P_2O_7$ glass. We identified three distinct types of zinc coordination: ^{IV}Zn, ^{V}Zn, and ^{VI}Zn. By creating models of these clusters, we determined that zinc is in the tetrahedral site within this structure. This conclusion was drawn via the evaluation of the structural stability of these models through global reactivity indices, indicating the stability of ^{IV}Zn polyhedra and enabling a further comprehensive understanding of the structural characteristics of $Zn_2P_2O_7$ glass material.

EXPERIMENTAL

The diphosphate glass, with the formula $Zn_2P_2O_7$, was prepared using the conventional melt quenching process. High-purity raw materials, $ZnCO_3$ (99.9 %) and $(NH_4)_2HPO_4$ (99.9 %), were accurately weighed based on their composition. Subsequently, they were mixed in a mortar with a pestle, then placed in a platinum crucible and heated to a temperature of 200°C for 4h. The obtained mixture was ground again and heated to the temperature of 400°C for 12h. These treatments were carried out to remove volatile substances such as water (H_2O), ammonia (NH_3), and carbon dioxide (CO_2). The resulting material was further ground and then melted at 1050°C. The final step in the process is the rapid cooling of this molten mass by quenching it onto a preheated metal plate. The X-ray diffraction spectrum of the glass sample was performed using a Siemens D5000 diffractometer in Bragg-Brentano reflection configuration. The source of X-rays is a CuKα copper anticathode (λ = 1.54056Å). The DSC measurements were performed using a SETARAM 121 apparatus. The thermogram was recorded under an argon atmosphere in a temperature range between 25°C and 800°C, with a heating rate of 10°C min^{-1}. The infrared analysis of our sample was carried out by means of a Bruker Platinium-ATR Fourier transform infrared spectrometer operating in transmittance mode, with a spectral range of measurement going from 400 to 4000 cm^{-1}. Raman spectroscopy data were collected using a Perkin-Elmer Spectrum GX spectrometer on a powdered glass sample with a 532 nm laser as the excitation wavelength. The laser power was optimized (0.5 mW) to avoid overheating of the sample. The spectrum was recorded in backscattered geometry in the wavenumber range between 150 cm^{-1} and 1400 cm^{-1}. The theoretical study of zinc diphosphate has been conducted using the density functional theory (DFT) with a restricted B3LYP exchange-correlation functional of Becke, 3-parameter, Lee-Yang-Parr with a 6-311G basis set. All calculations were performed using the GAUSSIAN 09 program package [25, 26].

RESULTS AND DISCUSSION

XRD diffraction and DSC investigation

Fig. 1a presents the X-ray diffraction spectrum of the prepared sample. The absence of Bragg peaks indicates the amorphous state of the sample. The recorded DSC thermogram is given in Fig. 1b. We note a change in the baseline, indicative of a glass transition. This finding affirms the glassy nature of the sample. The thermogram presents a single exothermic peak associated with crystallization process of the vitreous material. The glass transition temperature (T_g) value is found to be 720 K, the crystallization temperature (T_c) is at 871 K, and the onset of crystallization (T_x) occurs at 814 K.

Spectroscopic study

The experimental FT-IR spectrum of $Zn_2P_2O_7$ glass in the frequency range 400 - 1400 cm^{-1} is presented in Fig. 2. The obtained spectrum shows a broad and intense peak between 400 - 1200 cm^{-1}. This peak is composed of several overlapping Gaussian components.

To analyse this complex pattern, Spectra Manager software and a Gaussian-type function have been employed to deconvolve the spectrum and isolate these components for clearer analysis. The adjusted parameters are summarized in Table 1. The spectrum shows a low-frequency vibration mode recorded at around 400 cm^{-1} (389 cm^{-1}), which is attributed to the Zn–O bonds in the tetrahedral units ZnO_4. The bands recorded in the 480 - 530 cm^{-1} region is attributed to the symmetric deformation modes of the O–P–O angles in the Q_1 tetrahedra [37]. The band at 622 cm^{-1} corresponds to the symmetric stretching vibrations of the P–O–P in $P_2O_7^{4-}$ groups. The characteristic band located at 752 cm^{-1} is attributed to the asymmetric stretching of the P–O–P bridges. This region may also contain bands related to the pyrophosphate groups $P_2O_7^{4-}$ [38, 39]. The bands of symmetric and asymmetric stretching vibrations of the PO_3 groups are experimentally reported at higher frequencies in the range of 1000 cm^{-1} to 1200 cm^{-1} [40, 41]. Another band at 923 cm^{-1} is attributed to the asymmetric stretching vibrations of the P–O–Zn bond [42].

The experimental Raman spectrum of the $Zn_2P_2O_7$ glass is depicted in Fig. 3. The spectrum has been deconvoluted using the Spectra Manager program and a Gaussian-type function. The adjusted parameters are listed in Table 2. The bands at 601 cm^{-1} and 776 cm^{-1}, are respectively attributed to the symmetric and asymmetric stretching vibrations of the P–O–P in $P_2O_7^{4-}$ units [45].

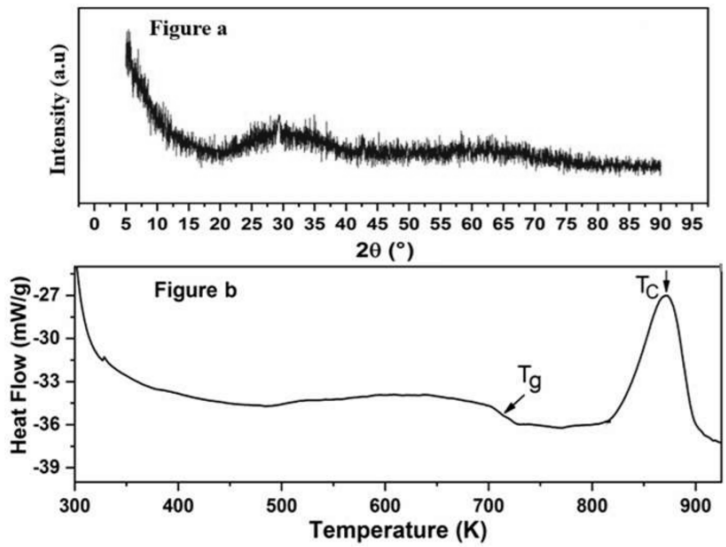

Fig. 1. (a) XRD pattern of $Zn_2P_2O_7$ glass, (b) A DSC thermogram displaying the glass transition temperature (T_g) and crystallization temperature (T_c).

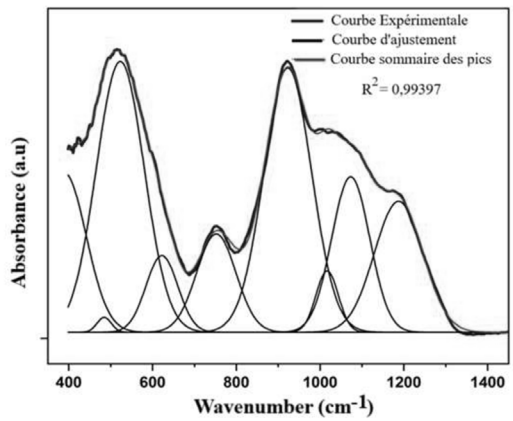

Fig. 2. Deconvolution of the recorded FT-IR spectrum of $Zn_2P_2O_7$ glass.

Table. 1. FT-IR spectrum components and their assignments for the $Zn_2P_2O_7$ glass.

Wavenumber, cm^{-1}	Assignment
389	Asymmetric stretching vibrations of the O–Zn–O angles in ZnO_4 tetrahedra [27]
485, 522	Symmetric deformation vibrations of the O–P–O angles in the tetrahedra Q_1 [28, 29]
622	Symmetric stretching vibrations of P–O–P [33]
752	Asymmetric stretching vibrations of P–O–P [31, 32, 35]
923	Asymmetric stretching vibrations of P–O–Zn [37]
1017, 1173	Symmetric stretching vibrations of PO_3 groups in Q_1 tetrahedra [30, 32, 34 - 36]
1187	Asymmetric and Symmetric stretching vibrations of PO_3 groups in Q_1 tetrahedra [30, 32, 34 - 36]

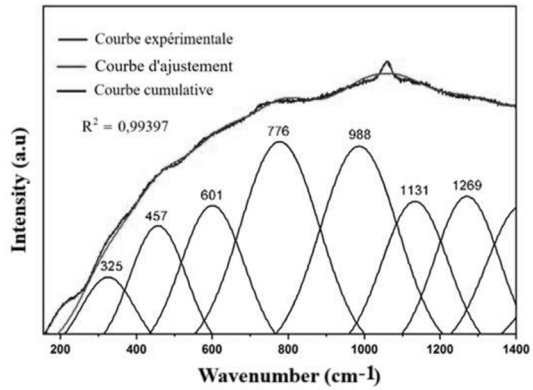

Fig. 3. RAMAN spectrum of $63ZnO\text{-}37P_2O_5$ glass.

Table 2. Raman $63ZnO\text{-}37P_2O_5$ glass spectrum components and their assignments.

Wavenumber, cm^{-1}	Assignment
325	Vibrations of symmetrical deformation of the angles O – Zn – O in ZnO_4 tetrahedra [27]
457	Vibrations of symmetrical deformation of the angles O – P – O in Q_1 tetrahedra [28, 29]
601	Symmetrical stretching vibrations of P – O – P [33]
776	Asymmetrical stretching vibrations of P – O – P [31, 32, 35]
988	Asymmetrical stretching vibrations of P – O – P [31, 32, 35]
1131	Symmetrical stretching vibrations of PO_2 groups in Q_2 tetrahedra [27, 46]
1269	Asymmetrical stretching vibrations of .PO_2 groups in Q_2 tetrahedra [27, 46]

The band at 457 cm^{-1} is related to the vibrations of symmetrical deformation of the angles O–P–O in Q_2 tetrahedra. These asymmetric stretching vibrations results also in the band located at 988 cm^{-1}. The bands of symmetric and asymmetric stretching vibrations of the PO_2 groups in the Q_2 tetrahedra are experimentally observed at higher frequencies between 1100 cm^{-1} to 1300 cm^{-1} [43]. Besides, the bands at 1400 cm^{-1} and 1850 cm^{-1} are due to the bending vibrations of H_2O [44]. However, the band at 325 cm^{-1} corresponds to the symmetric stretching vibrations of the tetrahedral Zn–O bonds [27].

Theoretical study of zinc-phosphate clusters

The experimental results presented in the previous section, reveal that the zinc ions are mainly linked to the Q_1 unit. This conclusion is drawn from observing the symmetric vibrations of P–O–P and the asymmetric vibrations of P–O–Zn. Moreover, the faintest band seen in both FT-IR and Raman spectra is attributed to the asymmetric vibrations of the O–Zn–O angles. Through these insights, we have distinguished three unique zinc clusters, namely ^{IV}Zn, ^{V}Zn, and ^{VI}Zn. The optimized structures and the average structural parameters of these clusters are given in Fig. 4 and Table. 3, respectively.

Fig. 4a illustrates the modeled ^{IV}Zn cluster, where zinc is centrally positioned within an oxygen tetrahedron, with a coordination number of IV. Non-bridging oxygens of two Q_1 structural units joined in short chains form this tetrahedron. At the start of the optimization process, a zinc ion was placed at the center of a perfect tetrahedral site. As the process evolved, this tetrahedral configuration began to change. The distances from the zinc to each oxygen atom (Zn–O) remained uniform at 1.959Å across the tetrahedron. Nonetheless, deviations were noted in the angles formed by oxygen-zinc-oxygen (O–Zn–O) bonds, with an average angle of 108.6 degrees. This deviation indicates a departure from the perfect tetrahedral shape. The interaction between zinc and oxygen significantly affects the phosphate structures around the zinc. The formation of Zn–O bonds leads to a noticeable decrease in the length of the phosphate-oxygen-zinc ($P–O_{Zn}$) bonds, from 1.651Å to 1.643Å. This contraction further influences the phosphate to non-bridging oxygen bonds ($P–O_{NBO}$), shortening them from 1.651Å to 1.620Å. Such alterations in the phosphate environment also affect the angles between oxygen-phosphate-oxygen (O–P–O) bonds. These adjustments bring the structural characteristics of the phosphate tetrahedra closer to those seen in Q_2 structural units. This suggests that the link between zinc and non-bridging oxygen converts Q_1 structural units into Q_2, at least geometrically.

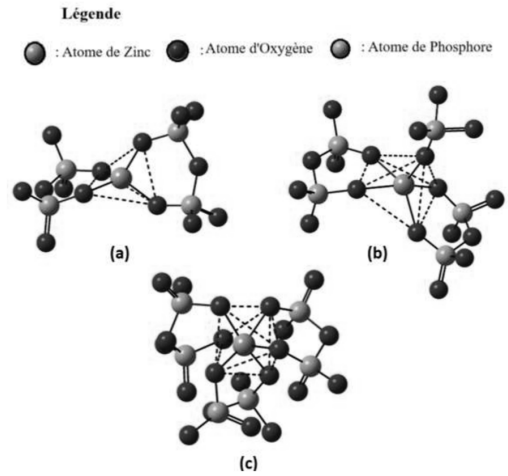

Fig. 4. Geometry optimized zinc-phosphate (a) tetrahedral, (b) pentahedral, and (c) octahedral clusters.

Table. 3. Calculated interatomic distances and angles of the different phosphate.

		^{IV}Zn	^{V}Zn	^{VI}Zn
Lengths (Å)	P=O	1.622	1.647	1.505
	$P–O_{NBO}$	1.620	1.624	1.709
	$P–O_{BO}$	1.743	1.762	1.703
	$P–O_{Zn}$	1.643	1.676	1.714
	Zn–O	1.959	2.142	1.913
Angles (°)	P–O–P	137.1	124.6	105.8
	P–O–Zn	137.6	152.5	111.0
	$O=P–O_{NBO}$	111.7	106.8	109.2
	$O_{NBO}–P–O_{BO}$	107.2	107.6	109.8
	$O_{BO}–P–Zn$	104.3	101.2	107.9
	$O_{NBO}–P–O_{Zn}$	113.0	115.4	109.4

In zinc-phosphate glasses, the existence of zinc in five-fold coordination cannot also be excluded. The optimized cluster, designated as ^{V}Zn, with zinc in coordination five is presented in Fig. 4b. The ^{IV}Zn cluster served as our initial point of reference, and we also introduced an isolated Q_0 structural unit into the zinc coordination. During the optimization process, the environment of the zinc formed by oxygen atoms this shell evolved into a bipyramidal structure with five-fold coordination. The Zn–O bond length increases to an average value of 2.142Å. The P–O_{Zn} distance between phosphorous and the oxygen coordinated with zinc surroundings is 1.676Å, longer than the P–O_{NBO} (1.651Å), and, shorter than the P–OBO (1.762Å). The zinc-phosphate cluster is also explored by considering zinc in an octahedral geometry formed by six Q_1 structural units (designated as ^{VI}Zn) (Fig. 4c). In this cluster, the four Zn–O bond lengths are 1.913Å. The reduction in bond lengths to P-O_{Zn} within the zinc coordination, observed previously, is also apparent in this configuration and accompanied by a notable decrease in the P-O-Zn angle to 111.0°. Upon inserting the zinc ion into the phosphate chains, one can observe that the P-O_{BO} distance for both ^{IV}Zn and ^{VI}Zn becomes 1.743Å and 1.703Å, respectively, closely resembling that of Q_2. Conversely, the angle O_{NBO}–P–O_{BO}, approximately 107.2°, is like that of the Q_1 unit [47, 48]. This indicates a complete transformation of the Q_1 structural unit to the Q_2 structural unit, with zinc occupying the tetrahedral site.

The electronic properties of the modelled structures were computed using Density Functional Theory (DFT), offering a detailed quantum mechanical perspective on their electronic configurations. The E_{HOMO} and E_{LUMO} were determined to derive the band gap (ΔE), indicative of electronic transitions and intrinsic conductivity. Chemical hardness (η) and softness (S) were calculated to evaluate the resistance to electron transfer, while the chemical potential (μ) and electrophilic index (ω) provided insight into the reactivity of these configurations [47, 48]. The obtained results are summarized in Table 4. The E_{HOMO} refers to the energy of the Highest Occupied Molecular Orbital. This indicates the energy level of the most energetic electrons in a molecule or solid-state structure. However, the E_{LUMO} energy corresponds to that of the Lowest Unoccupied Molecular Orbital. This is the energy level where an electron can be accepted. ΔE is the energy difference between LUMO and HOMO ($\Delta E=E_{LUMO}-E_{HOMO}$), also known as the band gap in solid-state physics. This parameter is an essential indicator of electronic stability and optical activity. ^{V}Zn cluster exhibits the smallest ΔE, suggesting higher reactivity and lower stability compared to ^{IV}Zn and ^{VI}Zn ones. This smaller band gap is typically associated with a higher density of states near the Fermi level, leading to increased conductivity. The other reactivity parameters including chemical potential (μ), softness (S), chemical hardness (η), and electrophilic index (ω) have been calculated based on the Eq. (1 - 4) [48, 49]:

$$\mu = \frac{E_{HOMO} + E_{LUMO}}{2} \quad (1)$$

$$\eta = \frac{E_{LUMO} - E_{HOMO}}{2} \quad (2)$$

$$S = \frac{1}{\eta} \quad (3)$$

$$\omega = \frac{\mu^2}{2\eta} \quad (4)$$

The chemical hardness (η) is an attribute that quantifies the resistance of a species to changing its electron density. ^{IV}Zn showed the highest η, implying greater stability and less reactivity, whereas ^{VI}Zn had the

Table 4. HOMO and LUMO energies, energy difference ΔE, chemical potential, softness, chemical hardness, and electrophile index of the ^{IV}Zn, ^{V}Zn, and ^{VI}Zn clusters.

Paramétres, eV, eV^{-1} / Structure	E_{HOMO} ± 0.0002	E_{LUMO} ± 0.0002	ΔE ± 0.0002	η ± 0.0002	S ± 0.0002	μ ± 0.0002	ω ± 0.0002
^{IV}Zn	4.9648	5.4734	0.5086	0.2543	3.9324	5.2191	53.5568
^{V}Zn	10.2982	10.7243	0.4261	0.2131	4.6926	10.5113	259.2385
^{VI}Zn	11.8812	12.4466	0.5654	0.2827	3.5373	12.1639	261.6917

lowest η, indicating higher reactivity. Correspondingly, the softness (S) of the clusters inversely mirrored their hardness, with ^{IV}Zn being the softest and, hence the most reactive. The chemical potential (μ) provides insights into the electron-donating or accepting capabilities. A lower μ in ^{V}Zn configuration suggests that it is more prone to gaining electrons, possibly enhancing its catalytic activity. Besides, the electrophilic index indicates the ability to act as an electrophile. ^{VI}Zn has the highest ω, suggesting a higher propensity to attract electrons compared to ^{IV}Zn and ^{V}Zn. These results indicate that the behavior of ^{VI}Zn is intricate, characterized by its minimal hardness contrasted with a pronounced electrophilic tendency, suggesting a distinctive pattern of reactivity. Moreover, the highlighted values indicate that ^{V}Zn clusters are likely the most reactive but the least stable, while ^{IV}Zn clusters show signs of lower reactivity and higher stability compared to the ^{V}Zn and ^{VI}Zn ones.

CONCLUSIONS

This article focuses on the study of the zinc diphosphate glass sample $Zn_2P_2O_7$. The results confirmed the amorphous and vitreous nature of this sample, as demonstrated by X-ray diffraction (XRD) and differential scanning calorimetry (DSC). Through a detailed examination of the experimental FT-IR and Raman spectra, it was observed that zinc is linked with two Q_1 units. Density functional theory (DFT) was employed to analyse the short-range structure of the $Zn_2P_2O_7$ glass. Three distinct types of short-range clusters were selected based on the experimental results, including ^{IV}Zn (tetrahedral), ^{V}Zn (pentahedral), and ^{VI}Zn (octahedral). The evaluation of the structural stability of these models using global reactivity indices confirmed that the structure based on ^{IV}Zn is more stable than those based on ^{V}Zn and ^{VI}Zn. This highlights the presence of zinc in the tetrahedral site of this structure. The theoretical FT-IR/RAMAN spectra simulated for the ^{IV}Zn model correlated well with the experimental results.

Authors' contributions

A.A., A.B.: Study conception and design; A.A.: data collection; A.A., A.B and L.B, analysis and interpretation of results; A.A., A.B. L. B: draft manuscript preparation. All authors reviewed the results and approved the final version of the manuscript. M.T. confirms sole responsibility for the following: study conception and design, data collection, analysis and interpretation of results, and manuscript preparation.

REFERENCES

1. B.C. Sales, Phosphate Glasses, MRS Bull, 12, 1987, 32-35.
2. 2. L.L. Hench, Bioceramics: from concept to clinic, Am. Ceram. Soc. Bull, 72, 1993, 93-98.
3. M. Ogino, L. Hench, Formation of calcium phosphate films on silicate glasses, J. Non-Cryst. Solids, international Congress on Glass, 38-39, 1980, 673-678.
4. J.P. Fletcher, R.J. Kirkpatrick, D. Howell, S.H. Risbud, ^{31}P Magic-angle spinning nuclear magnetic resonance spectroscopy of calcium phosphate glasses, J. Chem. Soc, Faraday Trans. 89, 1993, 3297-3299.
5. J.C. Knowles, Phosphate based glasses for biomedical applications, J. Mater. Chem, 13, 2003, 2395-2401.
6. E. A. Abou Neel, D.M. Pickup, S.P. Valappil, R.J. Newport, J.C. Knowles, Bioactive functional materials: a perspective on phosphate-based glasses, J. Mater. Chem, 19, 2009, 690-701.
7. M. Uo, M. Mizuno, Y. Kuboki, A. Makishima, F. Watari, Properties and cytotoxicity of water soluble Na_2O-CaO-P_2O_5 glasses, Biomaterials, 19, 1998, 2277-2284.
8. E. Gentleman., M.M. Stevens, R.G. Hill, D.S. Brauer, Surface properties and ion release from fluoridecontaining bioactive glasses promote osteoblast differentiation and mineralization in vitro, Acta Biomater, 9, 2013, 5771-5779.
9. D.M. Pickup, R.J. Newport, J.C. Knowles, Solgel phosphatebased glass for drug delivery applications, J. Biomater. Appl, 26, 2012, 613-622.
10. S.P. Valappil, D.M. Pickup, D.L. Carroll, C.K. Hope, J. Pratten, R.J. Newport, M.E. Smith, M. Wilson, J.C. Knowles, Effect of silver content on the structure and antibacterial activity of silver-doped phosphate-based glasses, Antimicrob. Agents Ch, 51, 2007, 4453-4461.
11. Y. Abe, M. Hayashi, T. Iwamoto, H. Sumi, L. Hench, Superprotonic conducting phosphate glasses

containing water, J. Non-Cryst. Solids, 351(2426), 2005, 2138-2141.
12. K. Kawaguchi, T. Yamaguchi, T. Omata, T. Yamashita, H. Kawazoe, J. Nishii, Phase separation and crystallization in sodium lanthanum phosphate glasses induced by electrochemical substitution of sodium ions with protons, Phys. Chem. Chem. Phys, 17, 2015, 22855-22861.
13. M. Szumera, I. Waclawska, Z. Olejniczak, Influence of B_2O_3 on the structure and crystallization of soil active glasses, J. Therm. Anal. Calorim, 99, 3, 2010, 879-886.
14. M. Szumera, I. Waclawska, Effect of molybdenum addition on the thermal properties of silicatephosphate glasses, J. Therm. Anal. Calorim, 109, 2, 2012, 649-655.
15. I. Waclawska, M. Szumera, P. Stoch, M. Sitarz, Structural role of Fe in the soil active glasses, Spectrochim. Acta A Mol. Biomol. Spectrosc, 79, 4, 2011, 728-732.
16. A. Royon, K. Bourhis, M. Bellec, G. Papon, B. Bousquet, Y. Deshayes, T. Cardinal, L. Canioni, Silver clusters embedded in glass as a perennial high-capacity optical recording medium, Adv. Mater, 22, 2010, 5282-5286.
17. J.R. Van Wazer, D.A. Campanella, Structure and properties of the condensed phosphates IV. Complex ion formation in polyphosphate solutions, J. Am. Chem. Soc, 72, 1950, 655-663.
18. R.K. Brow, Review: the structure of simple phosphate glasses, J. Non- Cryst. Solids, 263-264, 2000, 1-28.
19. U. Hoppe, A structural model for phosphate glasses, J. Non-Cryst. Solids. 195, 12, 1996, 138-147.
20. C.M. Shaw, J.E. Shelby, The effect of stannous oxide on the properties of stannous fluorophosphate glasses, Phys. Chem. Glass 29, 3, 1988, 87.
21. I.W. Donald, Preparation, properties and chemistry of glass-and glass-ceramic-to-metal seals and coatings, J. Mater. Sci., 28, 11, 1993, 2841-2886.
22. R.K. Brow, Nature of alumina in phosphate glass: I, properties of sodium aluminophosphate glass, J. Am. Ceram. Soc, 76, 4, 1996, 913-918.
23. R.K. Brow, C.M. Arens, X. Yu, D.E. Day, XPS study of iron phosphate glasses, 1994
24. U. Selvaraj, K.J. Rao, Transport properties of phosphomolybdate and phosphotungstate glasses, Philos. Mag. B, 58, 2, 1988, 203-216.
25. C. Lee, W. Yang, R.G. Parr, Development of the Colle-Salvetti correlation-energy formula into a functional of the electron density, Phys. Rev, B 37, 2, 1988, 785.
26. J. Harris, Simplied method for calculating the energy of weakly interacting fragments, Phys. Rev. B, 31, 4, 1985, 1770.
27. R. K. Brow, D.R. Tallant, S.T. Myers, C.C. Phifer, The short-range structure of zinc polyphosphate glass, J. Non-Cryst. Solids, 191, 1995, 45-55.
28. H. Doweidar, Y.M. Moustafa, K. El-Egili, I. Abbas, Infrared spectra of Fe_2O_3-PbO-P_2O_5 glasses, Vib. Spectrosc, 37, 2005, 91-96.
29. R.F. Bartholomew, Infrared and visible spectra. Journal of Non-Crystalline Solids, J. Non-Cryst. Solids, 7, 3, 1972, 221.
30. P. Shih, Properties and {FTIR} spectra of lead phosphate glasses for nuclear waste immobilization, Mater. Chem. Phys, 80, 1, 2003, 299-304.
31. A. Chahine, M. Et-tabirou, J. Pascal, FTIR and Raman spectra of the Na_2O-CuO-Bi_2O_3-P_2O_5 glasses, Mater. Lett, 58, 22-23, 2004, 2776-2780.
32. P. K. Jha, O. Pandey, K. Singh, FTIR spectral analysis and mechanical properties of sodium phosphate glassceramics, J. Mol. Struct., 1083, 2015, 278-285.
33. A. Shaim, M. Et-tabirou, Role of titanium in sodium titanophosphate glasses and a model of structural units. Mater Chem Phys, 80, 1, 2003, 63-67.
34. D. E. C. Corbrjdge, Infra-red analysis of phosphorus compounds, J. Appl. Chem, 6, 10, 1956, 456-465.
35. S. Stefanovsky, O. Stefanovsky, M. Remizov, E. Belanova, P. Kozlov, Y. Glazkova, A. Sobolev, I. Presniakov, S. Kalmykov, B. Myasoedov, FTIR and mssbauer spectroscopic study of sodiumaluminumiron phosphate glassy Materials for high level waste immobilization, J. Nucl. Mater., 466, 2015, 142-149.
36. L. Montagne, G. Palavit, G. Mairesse, ^{31}P MAS NMR and FT IR analysis of (50-x/2) $Na_2O.xBi_2O_3$. (50-x/2) P_2O_5 glasses, Phys. Chem. Glasses, 37, 5, 1996, 206.
37. G.B. Rouse Jr, P.J. Miller, W.M. Risen Jr, Mixed alkali glass spectra and structure, J. Non. Cryst. Solids, 28, 2, 1978, 193-207.
38. S. Bruni, F. Cariati, A. Corrias, P.H. Gaskell, A. Lai,

A. Musinu, G. Piccaluga, Short-Range Order of Sodium-Zinc, Sodium-Copper, and Sodium-Nickel Pyrophosphate Glasses by Diffractometric and Spectroscopic, Techniques, J. Phys. Chem, 99, 1995, 15229-15235.

39. S. Li, H. Liu, Y. Lu, Y. Qu, Y. Yue, Effects of barium oxide on structure and properties of calcium iron phosphate glasses, J. Non. Cryst. Solids, 450, 2016, 87-94.
40. A. Mekki, G.D. Khattak, L.E. Wenger, Structure and magnetic properties of lead vanadate glasses, J. Non-Cryst. Solids, 330, 1-3, 2003, 156.
41. J.J. Hudgens, R.K. Brow, D.R. Tallant, S.W. Martin, Raman spectroscopy study of the structure of lithium and sodium ultraphosphate glasses, J. Non-Cryst. Solids, 223, 1 - 2, 1998, 21-31.
42. P. Stoch, A. Stoch, M. Ciecinska, I. Krakowiak, M. Sitarz, Structure of phosphate and iron-phosphate glasses by DFT calculations and FTIR/Raman spectroscopy, J. Non-Cryst. Solids, 450, 2016, 48-60.
43. N. Sajai, A. Chahine, M. Et-Tabirou, M. Taibi, A. Mazzah, Structure and properties of (50-x)CaO-xPbO-50P_2O_5 metaphosphate glasses, J. Non-Cryst. Solids 347, 2004, 153-158.
44. J.V. Granadosa, F.G. Correaa, C.E.B. Díaz, Surface fractal dimensions and textural properties of mesoporous alkaline-earth hydroxyapatites, Appl. Surface Sci, 279, 2013, 97-102.
45. J. Schwarz, H. Tichá, L. Tichýa, R. Mertens, Physical properties of PbO-ZnO-P_2O_5 glasses. I. Infrared and Raman spectra, J. Optoelectron. Adv. M, 6, 2004, 737-746.
46. J. J. Hudgens, S. W. Martin, Glass transition and infrared spectra of low-alkali, anhydrous lithium phosphate glasses, J. Am. Ceram. Soc, 76, 1993, 1691.
47. A. EL Addali, A. EL Boukili, L. Boudad, H. Zouihri, M. Taibi, T. Guedira, Theoretical insights into phosphate chains: Density functional theory study and Zinc ion insertion reaction, J. Results Chem, 6, 2023, 101190.
48. A. El Addali, A. El Boukili, L. Boudad, M. Taibi, T. Guedira, Theoretical study of the phosphate units stability by the DFT B3LYP/6-311G quantum method, J. Chem. Technol. Metall., 31, 3, 2023, 477-485.
49. A. El Addali, A. El Boukili, L. Boudad, H. Zouihri, M. Taibi, T. Guedira, Study Of Vanadate Units Using Density Functional Théory: Electronic Properties and Reactivity. J. Chem. Technol., 32, 2, 2024, 294-303.